

A Jacobian-free Newton-Krylov method for cell-centred finite volume solid mechanics

Ivan Batistić^{1,2}, Pablo Castrillo^{1,3}, Philip Cardiff^{1*}

¹School of Mechanical and Materials Engineering, University College Dublin,
Ireland.

²Faculty of Mechanical Engineering and Naval Architecture, University of Zagreb,
Croatia.

³Instituto de Estructuras y Transporte, Facultad de Ingeniería, Universidad de la
República, Uruguay.

*Corresponding author. E-mail: philip.cardiff@ucd.ie

Abstract

This work extends the application of Jacobian-free Newton–Krylov (JFNK) methods to higher-order cell-centred finite-volume formulations for solid mechanics. While conventional cell-centred schemes are typically restricted to second-order accuracy, we present third- and fourth-order formulations that employ local least-squares reconstructions for gradient evaluation combined with Gaussian quadrature at cell faces for flux integration. These schemes enable accurate resolution of complex stress and deformation fields in both linear and nonlinear solid mechanics, while retaining the flexibility and geometric generality of finite-volume methods. A novel contribution of this study is the development and assessment of a JFNK solution strategy for these higher-order formulations, which eliminates the need to assemble and store large Jacobian matrices explicitly. Instead, we demonstrate that a compact-stencil approximate Jacobian can be effectively employed as a preconditioner, mirroring the efficiency gains observed in second-order frameworks. The proposed methodology is benchmarked across a suite of two- and three-dimensional test problems involving elastic and nonlinear materials, where key performance metrics, including accuracy, computational cost, memory usage, and robustness, are systematically evaluated. Results confirm that the higher-order formulations deliver substantial accuracy improvements over second-order schemes, while the JFNK approach achieves strong performance and scalability with only minimal modifications to existing segregated frameworks. These findings underscore the potential of combining higher-order finite-volume methods with JFNK solvers to advance the state of the art in computational solid mechanics. The implementations are openly released in the solids4foam toolbox for OpenFOAM, supporting further exploration and adoption by the community.

Keywords: Jacobian-free Newton-Krylov, higher-order, cell-centred finite volume method, solid mechanics, solids4foam, OpenFOAM

1 Introduction

Potential structure of this section:

1. Higher-order discretisation in computational solid mechanics remains relatively underexplored compared to fluid dynamics, despite its potential for improving accuracy and efficiency. Comment on 'why' we should care about higher order: potentially cheaper to achieve the same mesh error; potential to reduce the amount of data when running large models on HPC systems (where data is the bottleneck).
2. Recent research has demonstrated that higher-order accuracy can be achieved in cell-centred formulations through gradient reconstruction (e.g. least-squares approaches) and face integration techniques (e.g. Gaussian quadrature); however, their efficiency and ease of implementation in an industrial code are unexplored.
3. The solution strategy is a crucial factor: segregated iterative solvers remain the standard in finite-volume solid mechanics but often suffer from slow convergence and limited robustness, and they are efficient for higher orders, as shown by Demirdzic. Jacobian-free Newton–Krylov (JFNK) methods have emerged as a promising alternative, avoiding the need for explicit Jacobian construction while enabling quadratic convergence through Krylov subspace acceleration. In addition, the JFNK approach is well-suited for integration into existing segregated frameworks.
4. Our previous work established the feasibility and efficiency of JFNK for second-order cell-centred formulations, where a compact-stencil approximate Jacobian proved highly effective as a preconditioner. This study extends JFNK to third- and fourth-order cell-centred finite-volume formulations for linear and nonlinear solid mechanics, combining least-squares gradient reconstruction with Gaussian quadrature integration.
5. We demonstrate that the proposed approach significantly improves accuracy while retaining computational efficiency, and we show that compact-stencil Jacobians remain effective as preconditioners in the higher-order setting.
6. The aim of this paper is therefore twofold: to contribute to the relatively sparse literature on higher-order cell-centred finite-volume methods for solids, and to explore the synergy between such methods and Jacobian-free Newton–Krylov solution strategies.
7. pokazano je da se moze splitat surface topologija cv-a na surface skica molekule na symmetry planeu skica molekule na dirichlet boundariu sve jedna slika na kojoj je desni rub dirichlet, dole je symmetry a gore je neumann rub!

Philip comment: we should mention the importance of using consistent areas and volumes, e.g when discretising the volumetric terms we should use the same cell decomposition as we use to calculate the cell volume; the same applies for the face area integrals. Ivan noted this is required for non-flat faces to get the expected order of accuracy, e.g. on the irregular hexahedra/polyhedra meshes.

2 Mathematical Model

For arbitrary body of volume Ω bounded by surface Γ with outward facing unit normal \mathbf{n} the strong integral form of linear momentum in *total* Lagrangian form is:

$$\int_{\Omega_o} \rho_o \frac{\partial^2 \mathbf{u}}{\partial t^2} d\Omega_o = \oint_{\Gamma_o} (\mathbf{n}_o \cdot \mathbf{P}^T) d\Gamma_o + \int_{\Omega_o} \mathbf{f}_b d\Omega_o, \quad (1)$$

where ρ is density, \mathbf{u} is the displacement vector, \mathbf{P} is the first Piola–Kirchhoff stress tensor, and \mathbf{f}_b is a body force per unit volume, e.g., $\rho \mathbf{g}$, where \mathbf{g} is gravity. Subscript o is used to indicate quantities in the initial reference configuration. Through Nanson's formula it is possible to relate the first Piola–Kirchhoff stress tensor with the Cauchy $\boldsymbol{\sigma}$ stress tensor in the current configuration:

$$\mathbf{P} = J \boldsymbol{\sigma} \mathbf{F}^{-T}, \quad (2)$$

where \mathbf{F} is deformation gradient defined as $\mathbf{I} + (\nabla_o \mathbf{u})^T$ and J is its determinant $J = \det(\mathbf{F})$.

This work also considers linear geometry formulation, i.e. small strain assumption:

$$\int_{\Omega} \rho \frac{\partial^2 \mathbf{u}}{\partial t^2} d\Omega = \oint_{\Gamma} \mathbf{n} \cdot \boldsymbol{\sigma}_s d\Gamma + \int_{\Omega} \mathbf{f}_b d\Omega, \quad (3)$$

where $\boldsymbol{\sigma}_s$ is the engineering (small strain) stress tensor which coincide with Piola stress tensor.

Constitutive relation for Cauchy $\boldsymbol{\sigma}$ stress in Equations 2 and 3 is given by a chosen mechanical law. Mechanical laws considered in this work (Hooke's law, St. Venant-Kirchhoff, Mooney–Rivlin, neo-Hookean, and Guccione) are briefly outlined in Appendix A. The governing equations are complemented by boundary conditions, with three types considered here: prescribed displacement, prescribed traction, and symmetry.

3 High-order Finite Volume Discretisation

In this work, a finite volume discretization is employed to approximate the strong form of the governing equations. The computational points are located at the cell centroids, where the solution is treated as point-valued rather than cell-averaged. This type of discretization is commonly referred to as the deconvolution finite volume method [1, 2].

3.1 Solution domain discretisation

The spatial domain is partitioned into a finite set of contiguous convex polyhedral control volumes, each denoted by P . Representative control volumes in 2D and 3D settings is shown in Figure 1. The computational node associated with each cell P is positioned at the cell centroid \mathbf{x}_P , the cell volume is denoted by Ω_P , and the centroid of a neighboring control volume is denoted by N . Each control volume is bounded by a set of polygonal faces, which are categorized as follows:

- Internal faces — shared between adjacent control volumes. The centroid of an internal face is denoted by f , its outward unit normal vector by \mathbf{n}_f , and its face area by Γ_f .
- Boundary faces — located on the boundary of the spatial domain. The centroid of a boundary face is denoted by b , its outward unit normal vector by \mathbf{n}_b , and its surface area by Γ_b .

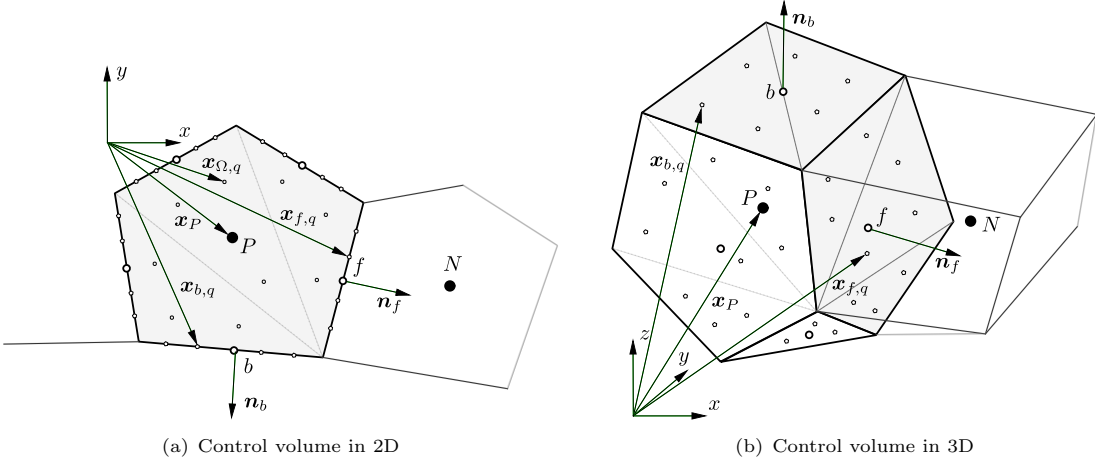


Fig. 1 Representative convex polyhedral cell P and neighbouring cell N .

Accurate and robust flux integration is required over these arbitrary polyhedral volumes. To facilitate this, each polygonal face f is subdivided into triangular subsurfaces, on which quadrature points \mathbf{x}_{fg} are defined for numerical flux evaluation. The fan triangulation method is adopted for face decomposition to minimise number of integration points. Although the computational mesh is always three-dimensional, two-dimensional problems are treated as planar, where the surface integration reduces to line integration along edges, therefore, no subdivision is required. Each cell volume P is decomposed into tetrahedral (in 3D) or triangular (in 2D) subelements, with volume quadrature points $\mathbf{x}_{\Omega,q}$ defined within each subelement. A key advantage of this geometric framework is its unified treatment of arbitrary polyhedral topologies—all control volumes are handled consistently using the same reconstruction and integration procedures. [Integration rules publications - cite them - maybe appendix?](#)

Before proceeding with the discretization of the volume and surface integrals, we introduce the following sets of cell faces. The set of internal faces is denoted by $\mathcal{F}_P^{\text{int}}$, and the set of boundary faces by $\mathcal{F}_P^{\text{bnd}}$. The boundary-face set $\mathcal{F}_P^{\text{bnd}}$ is further partitioned into three mutually disjoint subsets, $\mathcal{F}_P^{\text{bnd}} := \mathcal{F}_P^{\text{dip}} \cup \mathcal{F}_P^{\text{sym}} \cup \mathcal{F}_P^{\text{trac}}$, representing boundary faces where displacement ($\mathcal{F}_P^{\text{dip}}$), traction ($\mathcal{F}_P^{\text{trac}}$), or symmetry ($\mathcal{F}_P^{\text{sym}}$) conditions are prescribed. For convenience, we additionally define the set of non-traction boundary faces as $\mathcal{F}_P^{\text{non-trac}} := \mathcal{F}_P^{\text{dip}} \cup \mathcal{F}_P^{\text{sym}}$.

3.2 Surface Integrals

The surface integral term is discretised by integrating over quadrature points of each cell face:

$$\oint_{\Gamma_P} \mathbf{n} \cdot \boldsymbol{\sigma}_s \, d\Gamma_P = \sum_{f \in \mathcal{F}_P} \int_{\Gamma_f} \mathbf{n} \cdot \boldsymbol{\sigma}_s \, d\Gamma_f \approx \sum_{f \in \mathcal{F}_P^{\text{int}}} \mathbf{n}_f \cdot \left[\sum_{q=1}^{q=N_{f,q}} \alpha_q (\boldsymbol{\sigma}_s)_{f,q} \right] \Gamma_f + \sum_{b \in \mathcal{F}_P^{\text{non-trac}}} \mathbf{n}_b \cdot \left[\sum_{q=1}^{q=N_{f,q}} \alpha_q (\boldsymbol{\sigma}_s)_{b,q} \right] \Gamma_b + \sum_{b \in \mathcal{F}_P^{\text{trac}}} \mathbf{n}_b \cdot \sum_{q=1}^{q=N_{f,q}} \mathbf{T}_{b,q} \Gamma_b, \quad (4)$$

where Γ_P indicates the surface of cell P , vector $\mathbf{T}_{b,q}$ represents the prescribed traction at the traction boundary quadrature point, $N_{f,q}$ is the number of face quadrature points and α_q is quadrature weight. Subscript f,q indicates that quantity is calculated at quadrature point location $\mathbf{x}_{f,q}$. For non-triangular faces, face quadrature weights are scaled by the ratio of each triangle's area to the total face area, computed as the sum of all sub-triangle areas. Using a consistent definition of face area is essential, as inconsistency can degrade overall accuracy.

The stress tensor at a quadrature point $\mathbf{x}_{f,q}$, denoted $(\boldsymbol{\sigma}_s)_{f,q}$, is computed as a function of the displacement gradient according to the adopted mechanical constitutive law. For the case of engineering (Cauchy) stress, it is given by:

$$\boldsymbol{\sigma}_s(\mathbf{x}_{f,q}) = \mu(\nabla \mathbf{u})_{f,q} + \mu(\nabla \mathbf{u})_{f,q}^T + \lambda \text{tr}((\nabla \mathbf{u})_{f,q}) \mathbf{I} \quad (5)$$

where μ and λ are the Lamé parameters. Expressions for other constitutive laws are provided in Appendix A. The computation of the displacement gradient $(\nabla \mathbf{u})_{f,q}$ is shown in Section 3.5.

3.3 Volume Integrals

The volume integral is discretised by integrating over the cell volume quadrature points:

$$\int_{\Omega_P} \mathbf{f}_b \, d\Omega_P \approx \sum_{q=1}^{q=N_{f,q}} \beta_q (\mathbf{f}_b)_{\Omega,q} \Omega_P, \quad (6)$$

where $N_{f,q}$ is the number of cell quadrature points and β_q are the corresponding quadrature weights. Similarly, the inertia term (e.g. left-hand side term of Equation (3)):

$$\int_{\Omega_P} \rho \frac{\partial^2 \mathbf{u}}{\partial t^2} \, d\Omega_P \approx \sum_{q=1}^{q=N_{u,q}} \gamma_q \boldsymbol{\rho}_{\Omega,q} \left(\frac{\partial^2 \mathbf{u}}{\partial t^2} \right)_{\Omega,q} \Omega_P, \quad (7)$$

where $N_{u,q}$ and γ_q are quadrature points and corresponding weights used for inertia term integration. Subscript Ω,q is used to denote that quantity is calculated at quadrature point location $\mathbf{x}_{\Omega,q}$.

To evaluate these integrals over arbitrary polyhedral cells, the control volume is partitioned into a set of non-overlapping tetrahedra using the face subdivisions already defined for surface

integration. Each tetrahedron is formed by connecting the cell centroid P with one of the triangular faces, as illustrated in Figure 2. The cell partition is resolved at the quadrature weight calculation

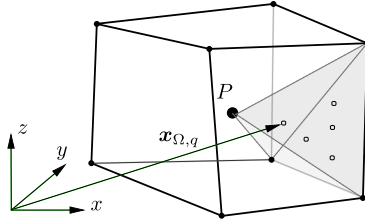


Fig. 2 Volume integration, cell decomposition into tetrahedral elements

level, where the integration weights are scaled by the ratio of its host tetrahedron's volume to the total cell volume. As in the computation of face quadrature weights, it is crucial to use a consistent cell volume [1].

3.4 Stabilisation Scheme

The evaluation of the surface term (diffusive flux) requires estimates of the solution gradient at the quadrature points $\mathbf{x}_{f,q}$ of a face. The most common approach is to average the gradients reconstructed from each side of a quadrature point, either using arithmetic averaging or interpolation with geometrically weighted coefficients. In the present work, the solution gradient is evaluated directly at the quadrature points, eliminating the need for such interpolation. However, as in the aforementioned averaging-based approaches, the discretisation of the diffusive flux may lead to numerical instabilities, manifested as zero-energy (checkerboard-type) modes. To suppress these high-frequency oscillations, an appropriate stabilisation (damping) must be introduced.

The most widely used stabilization technique in the finite-volume framework is the Rhie–Chow type stabilization [3], which is second-order accurate [4]. Since this limits the overall convergence rate to second order, it is not suitable for the present high-order discretisation. Instead, we employ an α -damping scheme [5], which preserves the designed high-order convergence of the method [6]. This damping is introduced in the form of an additional traction term \mathbf{t}_s , defined as a function of the solution jump between the values extrapolated from the centroids of the two cells sharing a common face:

$$\mathbf{t}_s = \alpha \frac{\bar{K}}{|\mathbf{d}_{PN} \cdot \mathbf{n}_f|} (\mathbf{u}_{fN}^* - \mathbf{u}_{fP}^*) \quad (8)$$

where α is scale factor and \bar{K} a stiffness-type parameter that gives the stabilisation an appropriate scale and dimension. It is calculated using Lamé parameters $\bar{K} = 2\mu + \lambda$, following previous works [7–9]. The vector \mathbf{d}_{PN} connects the centroid of cell P with that of its neighboring cell N , while the product $\mathbf{d}_{PN} \cdot \mathbf{n}_f$ serves as a skewness measure, increasing the damping on highly skewed cells [6]. The quantities \mathbf{u}_{fN}^* and \mathbf{u}_{fP}^* denote the displacements at the face center f , extrapolated from the cell centers using the derivatives evaluated at N and P , respectively:

$$\begin{aligned} \mathbf{u}_{fN}^* &= \mathbf{u}_N + \mathbf{d}_{Pf} \cdot (\nabla \mathbf{u})_N + \frac{1}{2} \mathbf{d}_{Nf}^2 : (\nabla \nabla \mathbf{u})_N + \frac{1}{6} \mathbf{d}_{Nf}^2 :: (\nabla \nabla \nabla \mathbf{u})_N, \\ \mathbf{u}_{fP}^* &= \mathbf{u}_P + \mathbf{d}_{Pf} \cdot (\nabla \mathbf{u})_P + \frac{1}{2} \mathbf{d}_{Pf}^2 : (\nabla \nabla \mathbf{u})_P + \frac{1}{6} \mathbf{d}_{Pf}^2 :: (\nabla \nabla \nabla \mathbf{u})_P, \end{aligned} \quad (9)$$

where $\mathbf{d}_{Pf} = \mathbf{x}_f - \mathbf{x}_P$ and $\mathbf{d}_{Nf} = \mathbf{x}_f - \mathbf{x}_N$ represent the vectors from the cell centers to the face center. The second and third derivatives in Equation (9) are employed only for third- and fourth-order discretizations, respectively, and their computation is described in Section 3.5.

The damping contribution is added to the surface integral in Equation (4), for internal faces and boundary faces on which displacement is prescribed:

$$\sum_{f \in \mathcal{F}_P^{\text{int}} \cup \mathcal{F}_P^{\text{disp}}} \mathbf{t}_s \Gamma_f = \sum_{f \in \mathcal{F}_P^{\text{int}}} \alpha \frac{\bar{K}}{|\mathbf{d}_{PN} \cdot \mathbf{n}_f|} (\mathbf{u}_{fN}^* - \mathbf{u}_{fP}^*) \Gamma_f + \sum_{b \in \mathcal{F}_P^{\text{disp}}} \alpha \frac{\bar{K}}{|\mathbf{d}_{Pb} \cdot \mathbf{n}_b|} (\mathbf{u}_b - \mathbf{u}_{fP}^*) \Gamma_b, \quad (10)$$

where \mathbf{u}_b is the prescribed displacement and $\mathbf{d}_{Pb} = \mathbf{x}_b - \mathbf{x}_P$.

3.5 High order interpolation scheme

3.6 Stencil

slika lijevo (internal + boudnary molecule) Slika desno cell centred molecule Slka ispod za simetriju kako je implementirana

3.7 Weight function

$$w(\mathbf{x}, \mathbf{x}_N, k) = \frac{e^{-\tilde{d}^2 k^2} - e^{-k^2}}{1 - e^{-k^2}}, \quad (11)$$

where $\tilde{d} = \frac{d}{d_s}$

3.8 Boundary conditions

4 Solution Algorithm

4.1 Jacobian-free Newton-Krylov Algorithm

5 Test Cases

root mean square error

$$L_2 = \frac{1}{N_c} \sum_{i=1}^{N_c} |\Delta\phi_i|, \quad (12)$$

and infinity norm representing the maximum absolute error

$$L_{\inf} = \max_{1 \leq i \leq N_c} |\Delta\phi_i|, \quad (13)$$

where $\Delta\phi_i$ is the difference between expected and predicted solutions and N_c is the overall number of computational points, i.e. cells. Both norms are calculated for displacement magnitude $|\mathbf{u}| = \sqrt{u_x^2 + u_y^2 + u_z^2}$ and von Mises stress:

$$\sigma_{ekv} = \sqrt{\frac{1}{2} [(\sigma_{xx} - \sigma_{yy})^2 + (\sigma_{yy} - \sigma_{zz})^2 + (\sigma_{zz} - \sigma_{xx})^2] + 3(\sigma_{xy}^2 + \sigma_{yz}^2 + \sigma_{zx}^2)} \quad (14)$$

5.1 Case 1: Order Verification via the Manufactured Solution Procedure

The first test case consists of a 0.2×0.2 m square or $0.2 \times 0.2 \times 0.2$ m cube with linear elastic ($E = 200$ GPa, $\nu = 0.3$) properties. A manufactured solution for displacement (Figure 9(a)) is employed in the form of polynomial, trigonometric [10] or mixed form [11]:

- 2D

$$\mathbf{u} = \begin{pmatrix} e^{x^2} \sin(y) \\ \ln(3+y) \cos(x) + \sin(y) \\ 0. \end{pmatrix} \quad (15)$$

- 3D - polynomial

$$\mathbf{u} = \begin{pmatrix} a_x(x^3 + xy^2) \\ a_y(y^3 + yz^2) \\ a_z(z^3 + zx^2) \end{pmatrix} \quad (16)$$

where $a_x = 1 \mu\text{m}$, $a_y = 1 \mu\text{m}$, and $a_z = 1 \mu\text{m}$.

- 3D - trigonometric

$$\mathbf{u} = \begin{pmatrix} a_x \sin(4\pi x) \sin(2\pi y) \sin(\pi z) \\ a_y \sin(4\pi x) \sin(2\pi y) \sin(\pi z) \\ a_z \sin(4\pi x) \sin(2\pi y) \sin(\pi z) \end{pmatrix} \quad (17)$$

where $a_x = 2 \mu\text{m}$, $a_y = 4 \mu\text{m}$, and $a_z = 6 \mu\text{m}$.

The Cartesian coordinates are given by x , y and z . The corresponding manufactured body force term (\mathbf{f}_b in Equation 3) can be found in authors previous publication [4] or obtained by manufactured solution procedure.

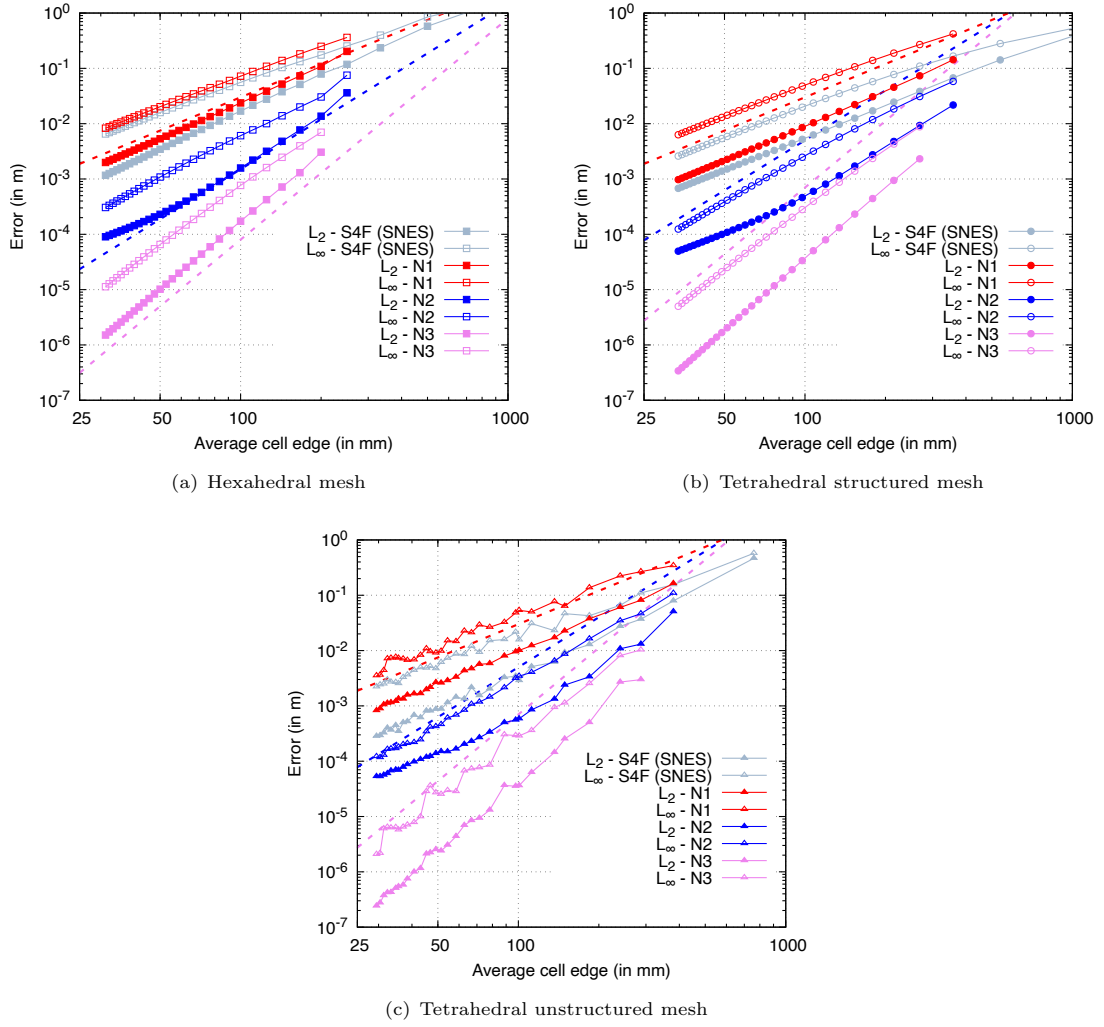


Fig. 3 Manufactured solution cube (2D case): error convergence for displacement magnitude

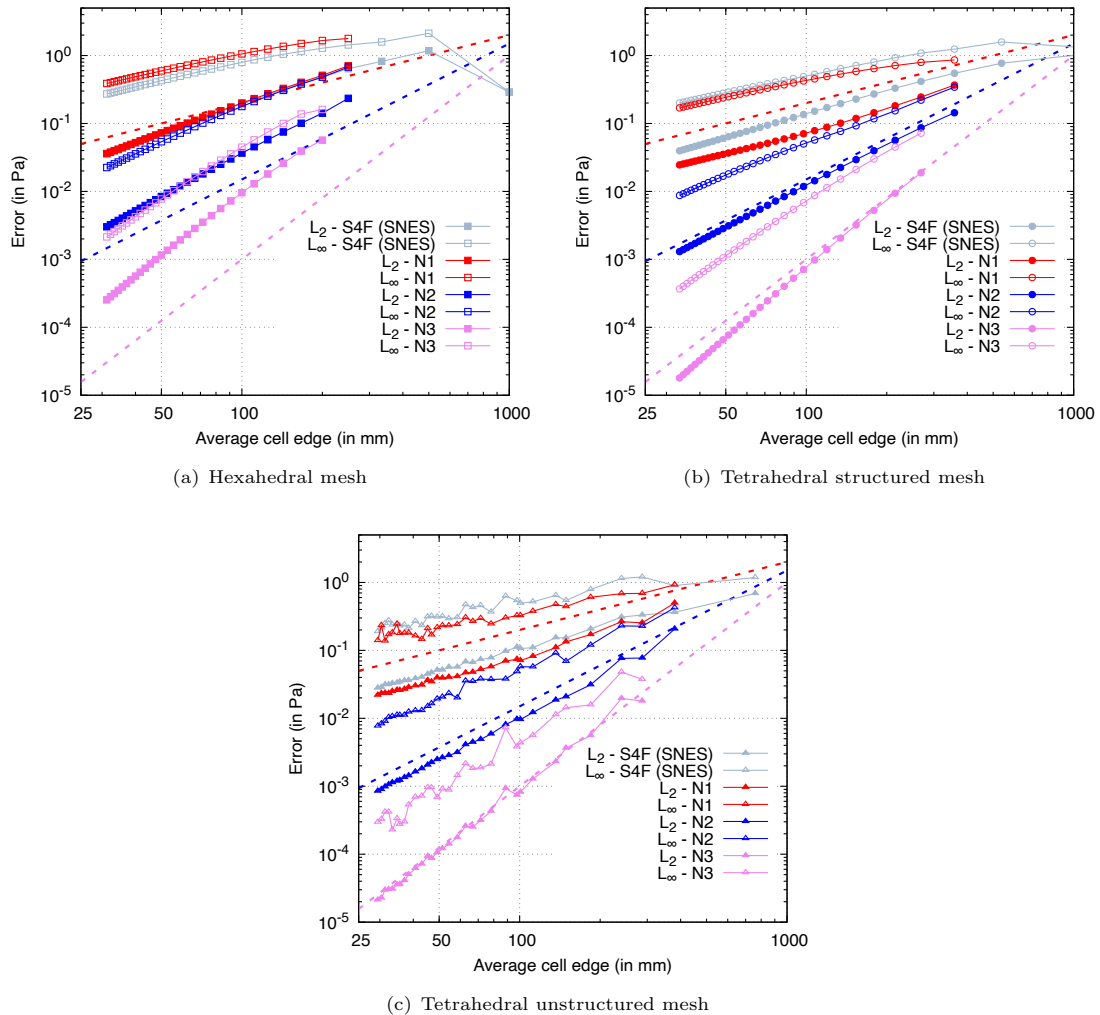


Fig. 4 Manufactured solution cube (2D case): error convergence for stress magnitude

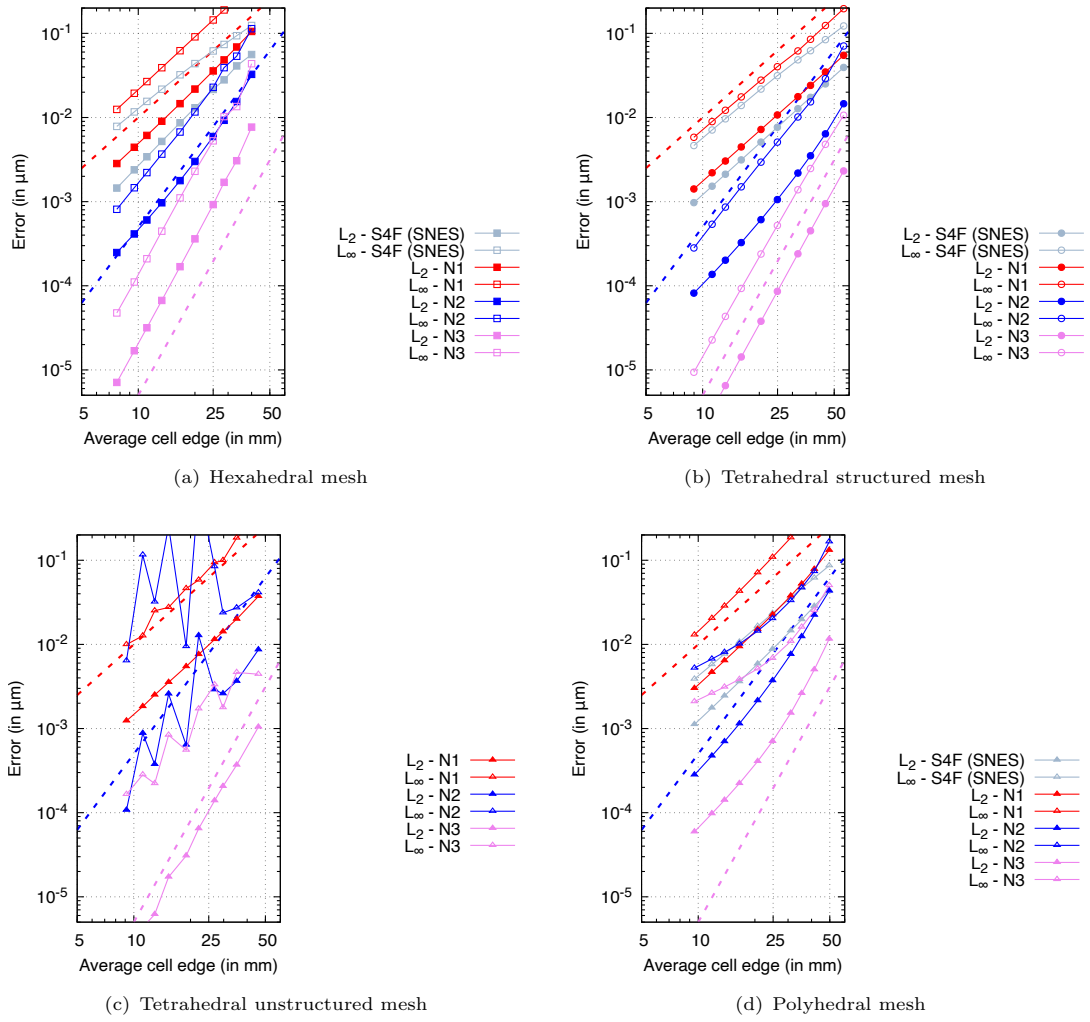


Fig. 5 Manufactured solution cube (3D case): error convergence for displacement magnitude

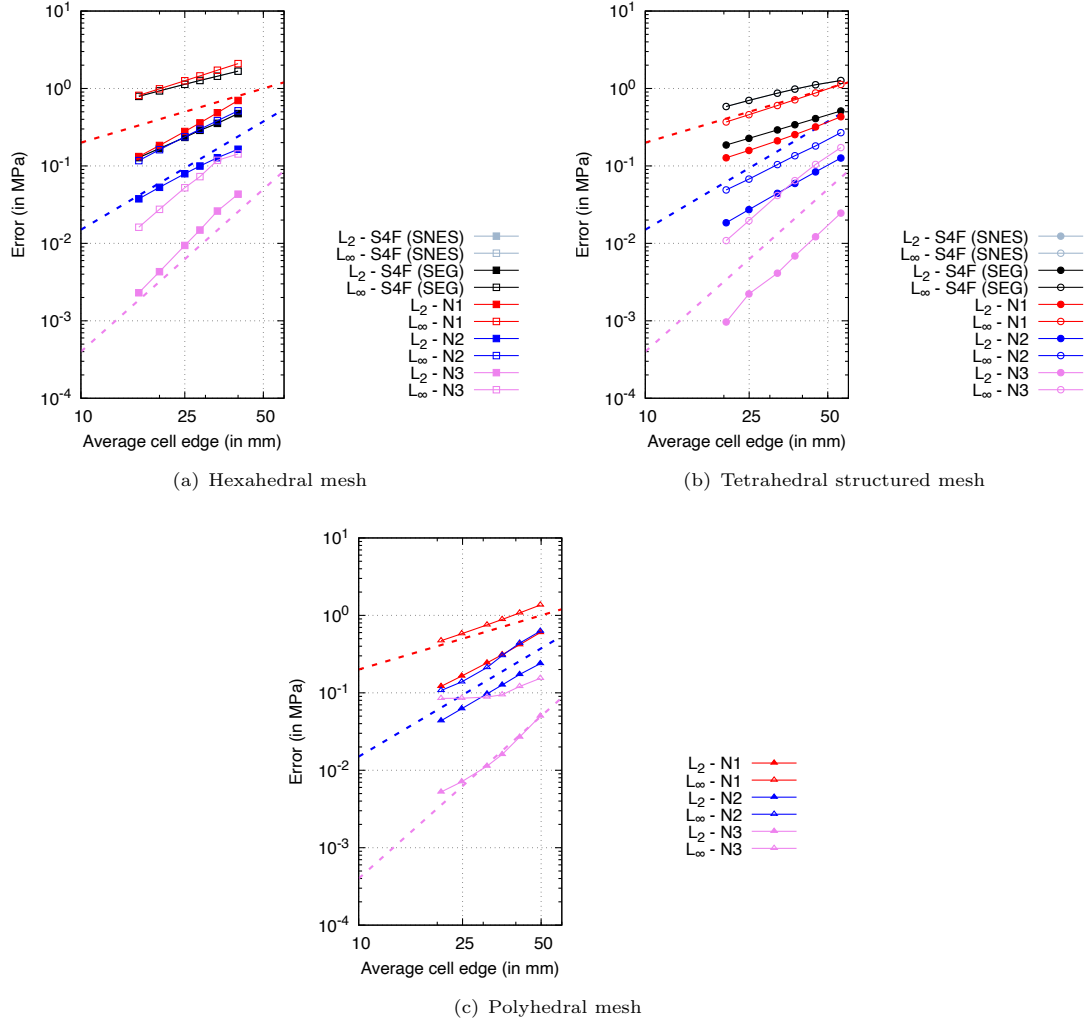


Fig. 6 Manufactured solution cube (3D case): error convergence for stress magnitude

5.2 Case 2: Cantilever beam

The test case geometry, shown in Fig. 6(a), is a rectangular beam with dimensions of $2 \text{ m} \times 0.2 \text{ m}$, a Young's modulus of $E = 200 \text{ GPa}$, and a Poisson's ratio of $\nu = 0.3$. The top and bottom boundaries of the beam are traction-free, and plane strain conditions are assumed. The left end of the beam is constrained by the analytical displacement, while the right end is subjected to the corresponding analytical traction of $(0, 1) \text{ MPa}$. This setup enables quantification of the difference between the predicted displacement and the analytical solution as a measure of convergence across the entire domain, rather than only at the beam end. Convergence is assessed using 15 successively refined grids.

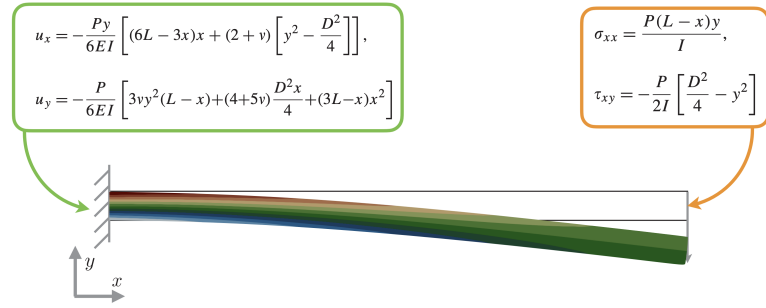


Fig. 7 Cantilever beam case: geometry and boundary conditions

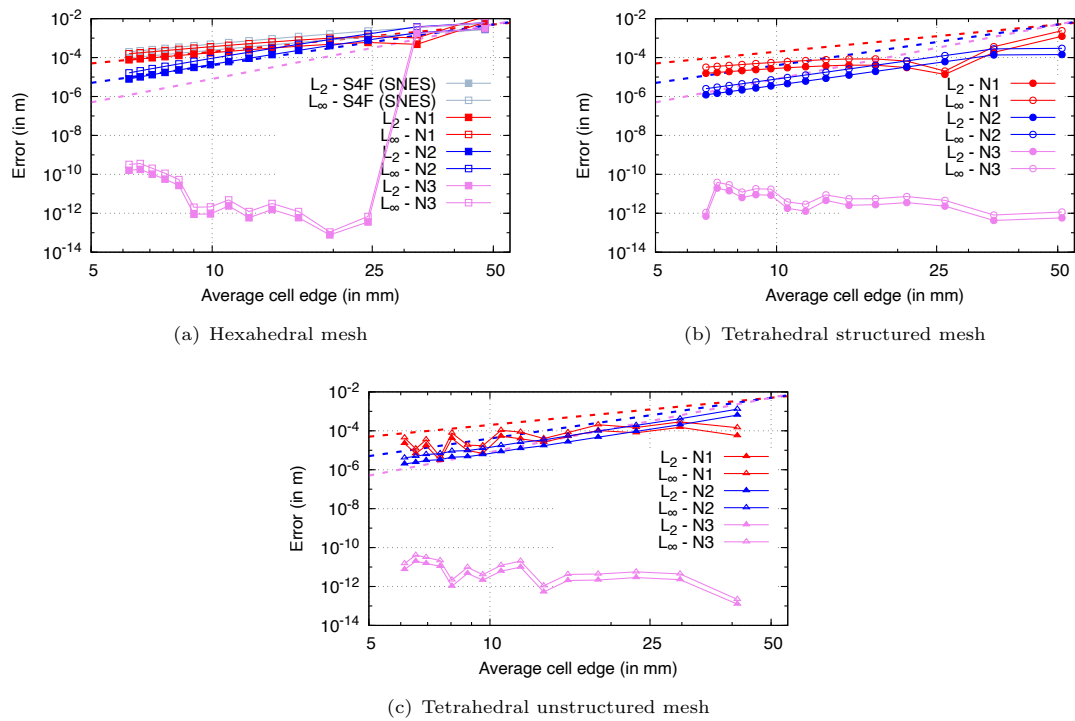


Fig. 8 Cantilever beam case: displacement magnitude discretisation errors

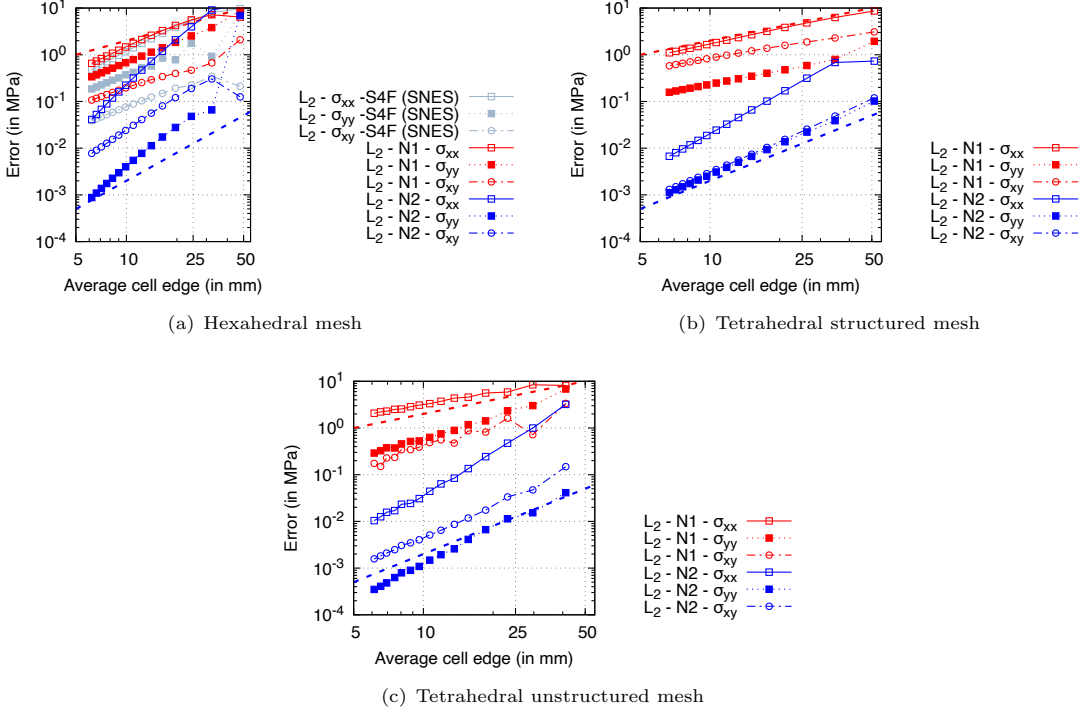


Fig. 9 Cantilever beam case: σ_{xx} , σ_{yy} , σ_{xy} stress discretisation errors. Results for $N = 3$ are not shown because stress error is around $\sim 10^{-12}$

5.3 Case 3: Internally pressurised thick-walled cylinder

In this case, a homogeneous thick-wall cylindrical pressure vessel with an inner radius $R_i = 7$ m, outer radius $R_o = 18.625$ m, and loaded internally with pressure $p = 100$ MPa is analysed. Two types of material are considered:

- i. Small strain, linear-elastic [12]: $E = 10$ GPa, $\nu = 0.3$.
- ii. Finite strain, Mooney-Rivlin law [13]: $c_{10} = 80$ MPa, $c_{01} = 20$ MPa, and $c_{11} = 0.0$ MPa and Poisson's ratio $\nu = 0.49$

The problem is considered plane stress, with the 2-D computational domain comprising a quarter of the cylinder geometry. The cylinder is discretised with series of unstructured tetrahedral grids. Gravitational and inertial effects are neglected. Linear elastic case is solved using one loading increment while hyperelastic case is solved using 100 equal loading increments. Analytical solutions are available in [14] and [15].

popraviiti slova na slici 8

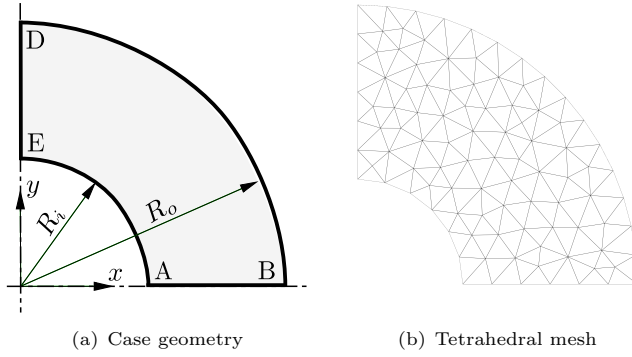


Fig. 10 Plate hole case geometry and mesh

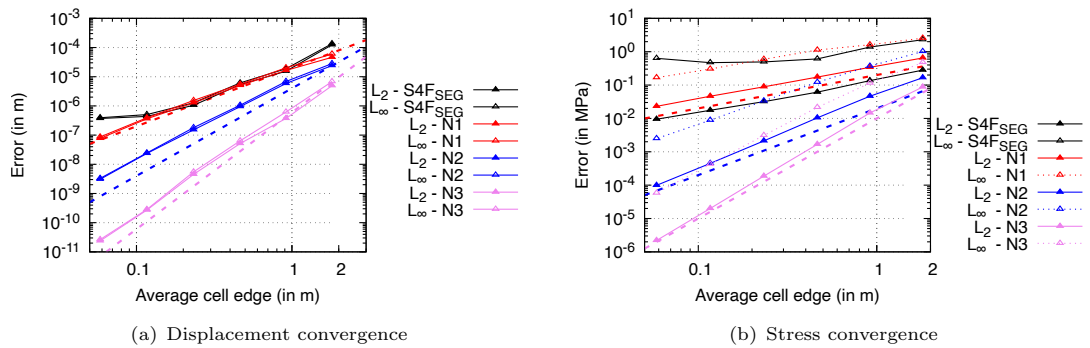


Fig. 11 Pressurised cylinder case: displacement and stress magnitude discretisation errors for linear elastic material

5.4 Case 4: Cooks membrane

5.5 Case 4: Plate hole

This benchmark problem consists of a thin, infinitely large plate with a circular hole, subjected to uniaxial tension. Owing to the symmetry of the geometry and loading, only one quarter of the plate is modeled as a finite domain. To minimize the influence of the finite computational boundaries, the exact tractions obtained from the analytical solution [16] are prescribed on the outer edges BC and CD. Symmetry boundary conditions are applied on boundaries AB and DE, while zero traction is specified on the hole boundary. The material properties are defined by a Young's modulus of $E = 200$ GPa and a Poisson's ratio of $\nu = 0.3$.

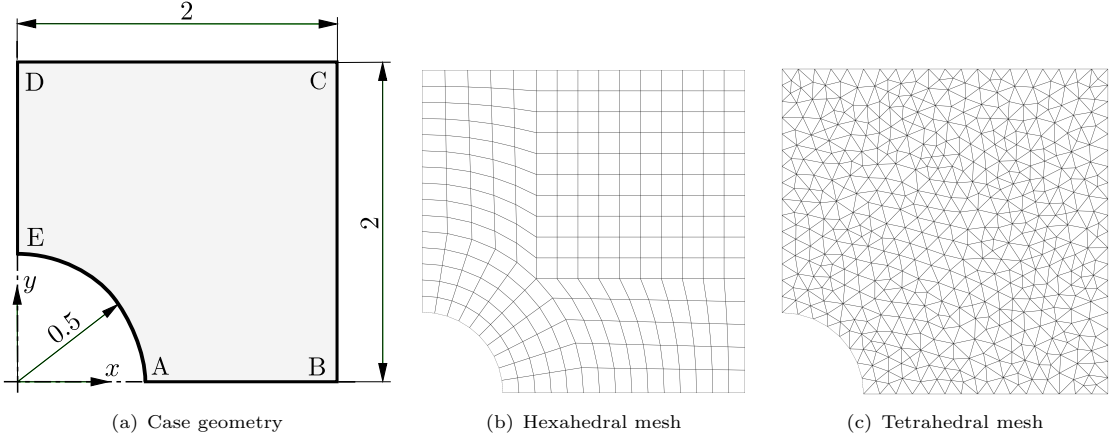


Fig. 12 Plate hole case geometry and mesh

Hexahedral mesh with N3 needs 20 neighbours to avoid ill conditioning. This results in lower slope for displacement but not affecting the stresses. I'm not sure why S4F results flatten on finer meshes.

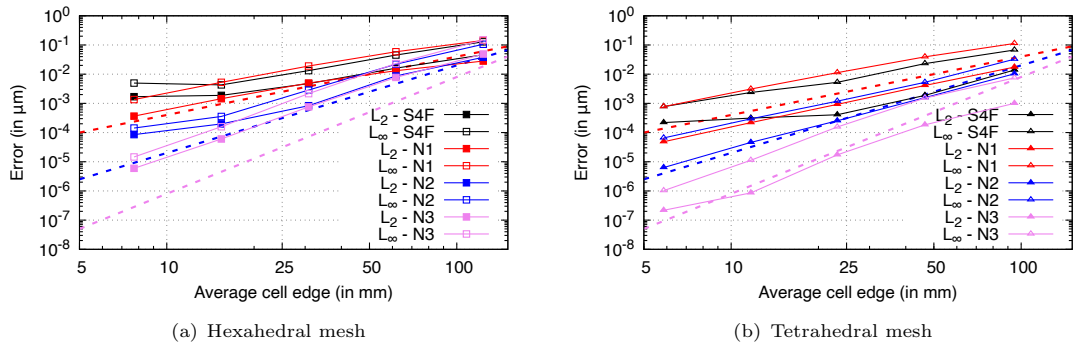


Fig. 13 Plate hole case: displacement magnitude discretisation errors

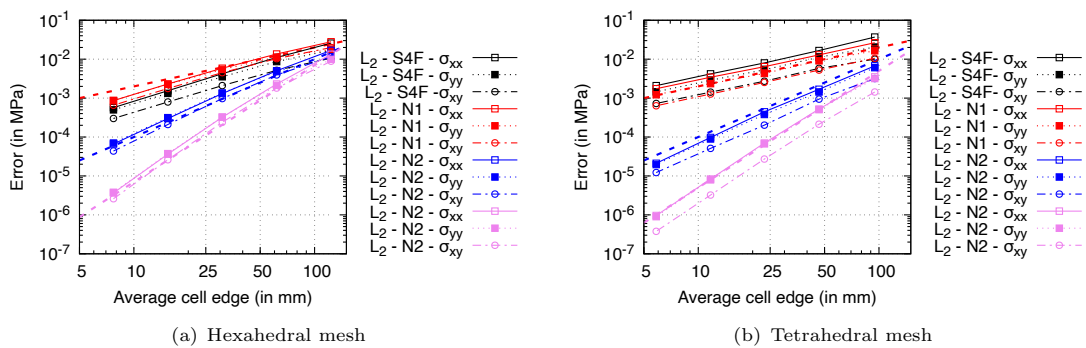


Fig. 14 Plate hole case: σ_{xx} , σ_{yy} , σ_{xy} stress discretisation errors.

5.6 Case 5: Elliptic plate

5.7 Case 6: Spherical cavity

5.8 Case 7: Idealised ventricle

5.9 Error-cost relationship

5.10 Stabilisation scheme effects

5.11 Effects of poor interpolation conditioning

Plate hole sa hex mrezom tu staviti i objasniti sto se desava u 2D-u sa kondicijskim brojem interpolacije

5.12 Code parallelisation

6 Conclusions

Data Availability. To be updated The codes presented are publicly available at <https://github.com/solids4foam/solids4foam> on the `feature-petsc-sn3s` branch, and the cases and plotting scripts are available at <https://github.com/solids4foam/solid-benchmarks>.

Acknowledgments. This project has received funding from the European Research Council (ERC) under the European Union’s Horizon 2020 research and innovation programme (Grant Agreement No. 101088740). Financial support is gratefully acknowledged from the Irish Research Council through the Laureate programme, grant number IRCLA/2017/45, from Bekaert through the University Technology Centre (UTC phases I and II) at UCD (www.ucd.ie/bekaert), from I-Form, funded by Science Foundation Ireland (SFI) Grant Numbers 16/RC/3872 and 21/RC/10295_P2, co-funded under European Regional Development Fund and by I-Form industry partners, and from NexSys, funded by SFI Grant Number 21/SPP/3756. Additionally, the authors wish to acknowledge the DJEI/DES/SFI/HEA Irish Centre for High-End Computing (ICHEC) for the provision of computational facilities and support (www.ichec.ie), and part of this work has been carried out using the UCD ResearchIT Sonic cluster which was funded by UCD IT Services and the UCD Research Office.

Appendix A Mechanical Laws

A.1 Linear Elasticity

The definition of engineering stress $\boldsymbol{\sigma}_s$ for linear elasticity can be given as

$$\begin{aligned}\boldsymbol{\sigma}_s &= 2\mu\varepsilon + \lambda \operatorname{tr}(\varepsilon) \mathbf{I} \\ &= \mu\nabla\mathbf{u} + \mu(\nabla\mathbf{u})^T + \lambda(\nabla \cdot \mathbf{u}) \mathbf{I}\end{aligned}\quad (\text{A1})$$

where λ is the first Lamé parameter, and μ is the second Lamé parameter, synonymous with the shear modulus. The Lamé parameters can be expressed in term of the Young's modulus (E) and Poisson's ratio ν as

$$\mu = \frac{E}{2(1+\nu)}, \quad \lambda = \frac{E\nu}{(1+\nu)(1-2\nu)} \quad (\text{A2})$$

A.2 St. Venant-Kirchoff Hyperelasticity

The St. Venant-Kirchoff model defines the second Piola-Kirchhoff stress \mathbf{S} as

$$\mathbf{S} = 2\mu\mathbf{E} + \lambda \operatorname{tr}(\mathbf{E}) \mathbf{I} \quad (\text{A3})$$

where, as before, λ is the first Lamé parameter, and μ is the second Lamé parameter. The Lagrangian Green strain \mathbf{E} is defined as

$$\mathbf{E} = \frac{1}{2}(\nabla\mathbf{u} + \nabla\mathbf{u}^T + \nabla\mathbf{u} \cdot \nabla\mathbf{u}^T) \quad (\text{A4})$$

The true stress can be calculated from the second Piola-Kirchhoff stress as

$$\boldsymbol{\sigma} = \frac{1}{J} \mathbf{F} \cdot \mathbf{S} \cdot \mathbf{F}^T \quad (\text{A5})$$

A.3 Neo-Hookean Hyperelasticity

The definition of true (Cauchy) stress $\boldsymbol{\sigma}$ for neo-Hookean hyperelasticity can be given as

$$\boldsymbol{\sigma} = \frac{\mu}{J} \operatorname{dev}(\bar{\mathbf{b}}) + \frac{\kappa}{2} \frac{J^2 - 1}{J} \mathbf{I} \quad (\text{A6})$$

where, once again, μ is the shear modulus, and κ is the bulk modulus. The bulk modulus can be expressed in terms of the Young's modulus (E) and Poisson's ratio ν as

$$\kappa = \frac{E}{3(1-2\nu)} \quad (\text{A7})$$

The volume-preserving component of the elastic left Cauchy–Green deformation tensor is $\bar{\mathbf{b}}$ is given as

$$\bar{\mathbf{b}} = J^{-2/3} \mathbf{b} = J^{-2/3} \mathbf{F} \cdot \mathbf{F}^T \quad (\text{A8})$$

In the limit of small deformations $\|\nabla \mathbf{u}\| \ll 1$, neo-Hookean hyperelasticity (Equation A6) reduces to linear elasticity (Equation A1).

A.4 Guccione Hyperelasticity

The Guccione et al. [17] hyperelastic law defines the second Piola-Kirchhoff stress as

$$\mathbf{S} = \frac{\partial Q}{\partial \mathbf{E}} \left(\frac{C}{2} \right) e^Q + \frac{\kappa}{2} \frac{J^2 - 1}{J} \mathbf{I} \quad (\text{A9})$$

where

$$Q(I_1, I_2, I_4, I_5) = c_t I_1^2 - 2c_t I_2 + (c_f - 2c_{fs} + c_t) I_4^2 + 2(c_{fs} - c_t) I_5 \quad (\text{A10})$$

$$\begin{aligned} \frac{\partial Q}{\partial \mathbf{E}} &= 2c_t \mathbf{E} + 2(c_f - 2c_{fs} + c_t) I_4 (\mathbf{f}_0 \otimes \mathbf{f}_0) \\ &\quad + 2(c_{fs} - c_t) [\mathbf{E} \cdot (\mathbf{f}_0 \otimes \mathbf{f}_0) + (\mathbf{f}_0 \otimes \mathbf{f}_0) \cdot \mathbf{E}] \end{aligned} \quad (\text{A11})$$

The scalars C , c_f , c_{fs} , and c_t are material parameters and invariants of the Green strain, $\mathbf{E} = \mathbf{F}^T \cdot \mathbf{F}$, are defined as

$$\begin{aligned} I_1 &= \text{tr}(\mathbf{E}), \quad I_2 = \frac{1}{2} [\text{tr}^2(\mathbf{E}) - \text{tr}(\mathbf{E} \cdot \mathbf{E})], \\ I_4 &= \mathbf{E} : (\mathbf{f}_0 \otimes \mathbf{f}_0), \quad I_5 = (\mathbf{E} \cdot \mathbf{E}) : (\mathbf{f}_0 \otimes \mathbf{f}_0) \end{aligned} \quad (\text{A12})$$

with \mathbf{f}_0 representing the unit fibre directions in the initial configuration.

Equation A5 is used to convert the second Piola-Kirchhoff stress to the true stress.

A.5 Mon-Rivlin - add here if used

Appendix B Body Force for the Method of Manufactured Solutions Case

The body force for the manufactured solution case is [10]:

$$f_b = \begin{pmatrix} \lambda [8a_y\pi^2 \cos(4\pi x) \cos(2\pi y) \sin(\pi z) \\ +4a_z\pi^2 \cos(4\pi x) \cos(\pi z) \sin(2\pi y) \\ -16a_x\pi^2 \sin(4\pi x) \sin(2\pi y) \sin(\pi z)] \\ +\mu [8a_y\pi^2 \cos(4\pi x) \cos(2\pi y) \sin(\pi z) \\ +4a_z\pi^2 \cos(4\pi x) \cos(\pi z) \sin(2\pi y) \\ -5a_x\pi^2 \sin(4\pi x) \sin(2\pi y) \sin(\pi z)] \\ -32a_x\mu_\pi^2 \sin(4\pi x) \sin(2\pi y) \sin(\pi z) \\ \\ \lambda [8a_x\pi^2 \cos(4\pi x) \cos(2\pi y) \sin(\pi z) \\ +2a_z\pi^2 \cos(2\pi y) \cos(\pi z) \sin(4\pi x) \\ -4a_y\pi^2 \sin(4\pi x) \sin(2\pi y) \sin(\pi z)] \\ +\mu [8a_x\pi^2 \cos(4\pi x) \cos(2\pi y) \sin(\pi z) \\ +2a_z\pi^2 \cos(2\pi y) \cos(\pi z) \sin(4\pi x) \\ -17a_y\pi^2 \sin(4\pi x) \sin(2\pi y) \sin(\pi z)] \\ -8a_y\mu_\pi^2 \sin(4\pi x) \sin(2\pi y) \sin(\pi z) \\ \\ \lambda [4a_x\pi^2 \cos(4\pi x) \cos(\pi z) \sin(2\pi y) \\ +2a_y\pi^2 \cos(2\pi y) \cos(\pi z) \sin(4\pi x) \\ -a_z\pi^2 \sin(4\pi x) \sin(2\pi y) \sin(\pi z)] \\ +\mu [4a_x\pi^2 \cos(4\pi x) \cos(\pi z) \sin(2\pi y) \\ +2a_y\pi^2 \cos(2\pi y) \cos(\pi z) \sin(4\pi x) \\ -20a_z\pi^2 \sin(4\pi x) \sin(2\pi y) \sin(\pi z)] \\ -2a_z\mu_\pi^2 \sin(4\pi x) \sin(2\pi y) \sin(\pi z) \end{pmatrix} \quad (B13)$$

Appendix C Meshes Used with the Method of Manufactured Solutions

References

- [1] Nishikawa, H., White, J.A.: An economical third-order nodal-gradient cell-centered finite-volume method for mixed-element grids. *Journal of Computational Physics* **540**, 114292 (2025) <https://doi.org/10.1016/j.jcp.2025.114292>
- [2] Nishikawa, H.: Economically high-order unstructured-grid methods: Clarification and efficient fsr schemes. *International Journal for Numerical Methods in Fluids* **93**(11), 3187–3214 (2021)

<https://doi.org/10.1002/fld.5028> <https://onlinelibrary.wiley.com/doi/pdf/10.1002/fld.5028>

- [3] Rhie, C.M., Chow, W.L.: Numerical study of the turbulent flow past an airfoil with trailing edge separation. *AIAA Journal* **21**(11), 1525–1532 (1983) <https://doi.org/10.2514/3.8284> <https://doi.org/10.2514/3.8284>
- [4] Cardiff, P., Armfield, D., Tuković, Batistić, I.: A Jacobian-free Newton-Krylov method for cell-centred finite volume solid mechanics (2025). <https://arxiv.org/abs/2502.17217>
- [5] Nishikawa, H.: Beyond interface gradient: A general principle for constructing diffusion schemes. In: 40th Fluid Dynamics Conference and Exhibit. AIAA, Chicago, Illinois, USA (2010). <https://doi.org/10.2514/6.2010-5093>. Published online: 13 Nov 2012
- [6] Nishikawa, H.: Robust and accurate viscous discretization via upwind scheme – i: Basic principle. *Computers & Fluids* **49**(1), 62–86 (2011) <https://doi.org/10.1016/j.compfluid.2011.04.014>
- [7] Tuković, Ž., Ivanković, A., Karač, A.: Finite-volume stress analysis in multi-material linear elastic body. *International Journal for Numerical Methods in Engineering* **93**(4), 400–419 (2013) <https://doi.org/10.1002/nme.4390> <https://onlinelibrary.wiley.com/doi/pdf/10.1002/nme.4390>
- [8] Cardiff, P., Tuković, Ž., Jaeger, P.D., Clancy, M., Ivanković, A.: A Lagrangian cell-centred finite volume method for metal forming simulation. *International Journal for Numerical Methods in Engineering* **109**(13), 1777–1803 (2017) <https://doi.org/10.1002/nme.5345> <https://onlinelibrary.wiley.com/doi/pdf/10.1002/nme.5345>
- [9] Cardiff, P., Karač, A., Jaeger, P.D., Jasak, H., Nagy, J., Ivanković, A., Tuković, Ž.: An open-source finite volume toolbox for solid mechanics and fluid-solid interaction simulations (2018) <https://doi.org/10.48550/arXiv.1808.10736> . <https://arxiv.org/abs/1808.10736>
- [10] Mazzanti, F.: Coupled vertex-centred finite volume methods for large-strain elastoplasticity. PhD thesis, University College Dublin (2024). For examination
- [11] Castrillo, P., Canelas, A., Schillaci, E., Rigola, J., Oliva, A.: High-order finite volume method for linear elasticity on unstructured meshes. *Computers & Structures* **268**, 106829 (2022) <https://doi.org/10.1016/j.compstruc.2022.106829>
- [12] Bijelonja, I., Demirdžić, I., Muzaferija, S.: A finite volume method for incompressible linear elasticity. *Computer Methods in Applied Mechanics and Engineering* **195**, 6378–6390 (2006)
- [13] Bijelonja, I., Demirdžić, I., Muzaferija, S.: A finite volume method for large strain analysis of incompressible hyperelastic materials. *International Journal for Numerical Methods in Engineering* **64**, 1594–1609 (2005)
- [14] Timoshenko, S., Goodier, J.: Theory of Elasticity. McGraw-Hill Company, Inc., New York (1970)
- [15] Green, A.E., Zerna, W.: Theoretical Elasticity. Courier Corporation, ??? (1992)

- [16] Demirdžić, I., Muzaferija, S., Perić, M.: Benchmark solutions of some structural analysis problems using finite-volume method and multigrid acceleration. International journal for numerical methods in engineering **40**(10), 1893–1908 (1997)
- [17] Guccione, J.M., Costa, K.D., McCulloch, A.D.: Finite element stress analysis of left ventricular mechanics in the beating dog heart. Journal of Biomechanics **28**(10), 1167–1177 (1995) [https://doi.org/10.1016/0021-9290\(94\)00174-3](https://doi.org/10.1016/0021-9290(94)00174-3)